RAIL FLAW IMAGING PROTOTYPE BASED ON IMPROVED ULTRASONIC SYNTHETIC APERTURE FOCUS METHOD

BY CHENGYANG HUANG* AND FRANCESCO LANZA DI SCALEA*†

ABSTRACT

This paper presents an experimental prototype developed for rail flaw imaging. This capability can help obtain quantitative information on detected flaws during manual flaw verification. Ultrasonic synthetic aperture focus (SAF) imaging has advantages over phased-array imaging for both speed and accuracy. The prototype developed is hosted in a portable and battery-powered carry-on size case. The probe is a linear ultrasonic array mounted on a wedge and with a position encoder to build 3D point clouds from 2D beamformed images. The prototype includes several advances over the basic SAF technique, including sparse subarray firing that allows fast imaging speeds (e.g., 25 Hz) without sacrificing image accuracy. Validation results are presented from scans performed on rail sections from the FRA rail defect library, which contains natural transverse defects and artificial end-drilled hole defects. The tests showed good accuracy in defect size and shape, as compared to the available ground truth information, for defects located away from the railhead corners. Additional developments are required to properly cover the head corners, and especially in the case of heavily worn rails.

KEYWORDS: nondestructive testing, ultrasonic imaging, synthetic aperture focus, SAF, phased arrays, rail flaws

* Experimental Mechanics & NDE Laboratory, Department of Structural Engineering, University of California at San Diego, La Jolla, CA 92093
† flanza@ucsd.edu

Materials Evaluation 82 (1): 51–59
https://doi.org/10.32548/2024.me-04371

Introduction

Internal rail flaws are a significant cause of train accidents. According to FRA's Safety Statistics data shown in Figure 1, in the past five years (2018–2022) detail fractures were responsible for as many as 222 derailments and damage cost of US$79 million (the highest cost of any other cause within the category of Track, Roadbed, and Structures). Transverse/compound fissures (TF) were responsible for 77 derailments and US$21 million in damage, and vertical split head (VSH) defects caused 83 derailments and ~US$20 million in damage. These three defects combined, therefore, caused as many as ~80 derailments per year and ~US$25 million in damage per year. The detection and quantification of these flaws is clearly of importance to railroad safety and efficiency.

The current manual verification of detected flaws consists of a simple ultrasonic pulse-echo test conducted using a handheld ultrasonic transducer with a wedge that is manually moved around the flaw in attempt to estimate the flaw size through a –6 dB threshold technique (Lanza di Scalea 2007). This process yields rail flaw sizing results that are highly subjective to the operator's judgement. An improved flaw verification would allow the generation of 3D ultrasound images of the internal flaw for an objective determination of flaw size and orientation. Knowledge of the correct flaw size can inform the most appropriate remedial actions, which can largely reduce the cost of rail maintenance and improve safety.

Current OEM portable systems exist for manual flaw imaging in structural components using ultrasonic techniques. These systems are based on phased array (PA) technology (Witte and Poudel 2016). As schematized in Figure 2, in PAs the transmission is sent to all channels that are appropriately delayed for physical focusing and steering at various depths. This means that (a) the PA hardware is fairly complicated because of the multiple digital-to-analog (D/A) output channels required; (b) the PA imaging speed is limited by the need to physically focus at different locations in the medium; and (c) the classical PA beamforming is only achieved in transmission through focused beams, which limits the lateral resolution. Conversely, synthetic aperture focus (SAF) techniques have been considered for defect imaging for various benefits over the PA methods (Drinkwater and Wilcox 2006). In a traditional SAF scheme, the transmission is sent to a single channel

(A)

TRAIN ACCIDENTS BY CAUSE FROM FORM FRA F 6180.54

MAJOR CAUSE= Track

Selections: Railroad - ALL
Region - All Regions
State - ALL, County - ALL
Derailment / All TRACK TYPES / T-ALL-Track, Roadbed and Structures
Time Frame: Jan 2018 To Dec 2022

Specific causes:	Total		Type of Accident	Reportable Damage		Casualty	
	Cnt	%	Der	Amount	%	Kld	Nonf
T001- Roadbed settled or soft	99	4.5	99	32,194,952	6.9	0	0
T002- Washout/rain/slide/etc. dmg -track	19	0.9	19	20,796,111	4.5	0	8
T099- Other roadbed defects	8	0.4	8	1,153,547	0.2	0	0
T101- Cross level of track irregular(joints)	45	2.1	45	3,541,392	0.8	0	0
T102- Cross level track irreg.(not at joints)	58	2.7	58	10,996,036	2.4	0	1
⋮							
T207- Detail fracture - shelling/head check	222	10.2	222	78,938,028	16.9	0	0
T220- Transverse/compound fissure	77	3.5	77	21,390,579	4.6	0	0
T221- Vertical split head	83	3.8	83	19,269,929	4.1	0	0

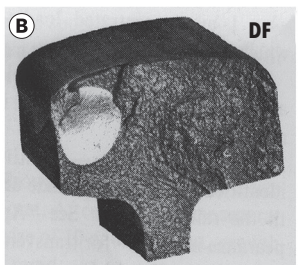

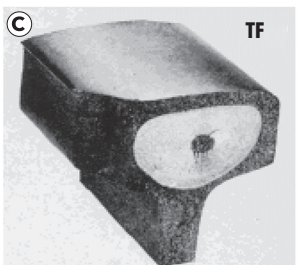

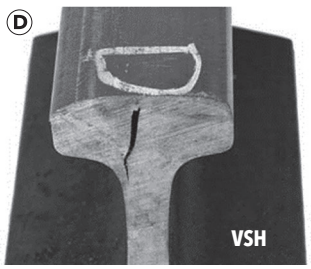

Figure 1. Examples: (a) FRA safety statistics data for all track, roadbed, and structures (2018–2022); (b) detail fracture (DF); (c) transverse fissure (TF); and (d) vertical split head (VSH).

at a time, and the focusing is done in post-processing both in transmissions and in receptions (two-way synthetic focusing) (Flaherty et al. 1967). This means that (a) the SAF hardware can be much simpler since only a few D/A output channels are required; (b) the SAF imaging speed can be increased by limiting the output channels; and (c) the SAF focusing is achieved in both transmission and reflection, leading to better resolution in a large inspection area.

It should be also mentioned that modern PA technology is utilizing elements of SAF in the ability to focus in reception through time backpropagation delay laws.

The objective of this paper is to present an experimental prototype system for 3D imaging of internal rail flaws using ultrasonic SAF techniques. An improved SAF beamforming scheme is proposed based on sparse subarray firing to provide high-contrast images in quasi real time (Huang and Lanza di Scalea 2022). A sophisticated post-processing routine is developed to enable automatic rail flaw quantification without the user's judgement. The prototype's hardware is packaged in a battery-powered storage case for portability and ruggedness. Validation tests were performed on a number of flawed rail sections from the FRA rail defect library managed by MxV Rail (formerly TTCI). The flaw images generated by the imaging prototype showed a good match compared to the ground truth established from rail break tests, especially in the case of natural transverse-type defects.

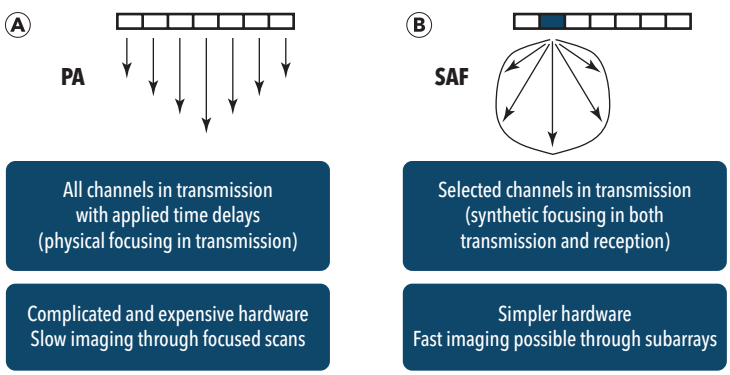

Figure 2. Ultrasound imaging technology: (a) conventional phased arrays vs. (b) synthetic aperture focusing.

The SAF Imaging Prototype

A portable imaging prototype was designed, assembled, and tested to enable handheld ultrasound imaging of rail flaws based on an enhanced SAF technique. As shown in Figure 3a, the hardware components of the imaging prototype were a multiplexer, a 12 V battery, a host computer, and a probe comprised of a transducer array, a wedge, and an encoder wheel. All the hardware components were screw fixed inside a carry-on size storage case. The multiplexer (a high-speed data acquisition system) that allowed multichannel data acquisition controlled the pulsed emission and reception to/from the array. A 12 V battery was used to support the multiplexer for up to 8 h of autonomous operation. The probe was composed of a transducer array, a shear wedge, and an encoder, as shown in Figure 3b. The transducer was a 64-element longitudinal (L) wave linear array with a central frequency at 2.25 MHz. The array was attached to a 55-degree wedge to generate directional shear (S) waves in the rail steel. The encoder recorded

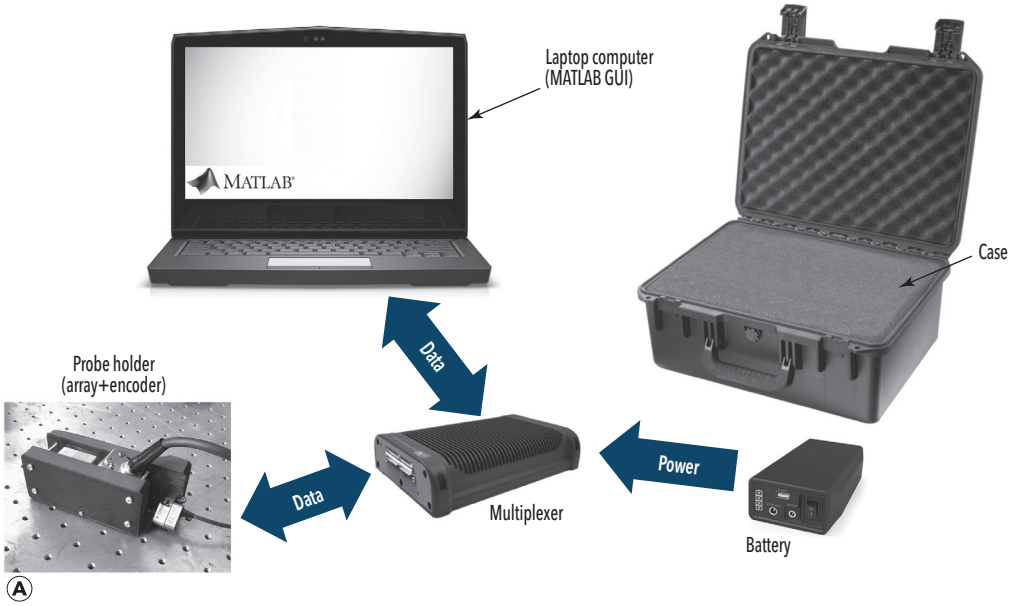

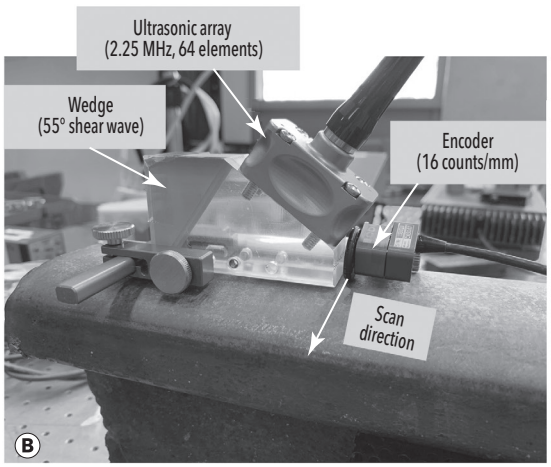

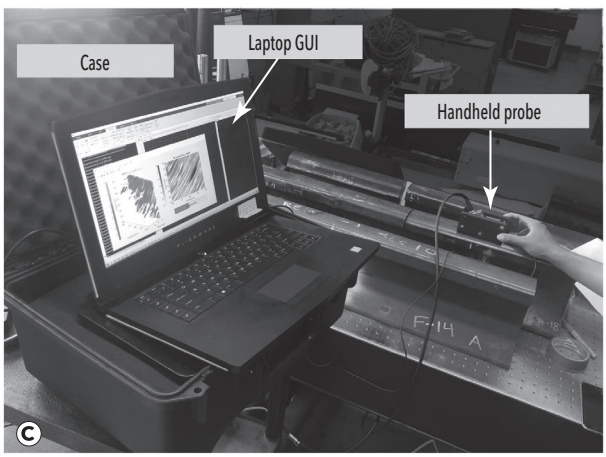

Figure 3. Portable imaging prototype: (a) main components; (b) array-wedge probe; (c) prototype during scanning of a rail section in the laboratory.

the transverse position of the probe when scanned on the rail surface, with a resolution of 16 counts/mm. The encoder allowed the system to create 3D images from the individual 2D scans. The array was coupled to the wedge using conventional ultrasonic gel couplant. The couplant was also applied at the wedge/rail interface to compensate for the impedance mismatch. A graphical user interface (GUI) platform was developed on a standard commercial laptop with a GPU available for parallel computation. All steps of the signal processing algorithms were programmed and automated in the GUI platform, which enabled flexible configuration and result analysis for the user's convenience. As shown in Figure 3c, during testing the user simply moves the probe on the surface of the rail section, and 3D images of the scanned area are displayed in quasi real time in the GUI.

Specific features of the image reconstruction algorithms that were developed and implemented in the prototype are discussed in detail in the following subsections.

Time Backpropagation Beamforming with a Transducer Wedge

The time backpropagation algorithm (also known as delay-and-sum or DAS algorithm) is widely used in SAF imaging (Jensen et al. 2006). Dynamic focus is achieved both in transmission and in reception by considering the ray path connecting the transmitting transducer element, the focus point, and the receiving transducer element. An image is built by summing the backpropagated signals through all transmitter-receiver pairs of the transducer array. Considering transmitters $i = 1, 2,\ldots, M$ and receivers $j = 1, 2,\ldots, N$, the DAS beamformed SAF image is constructed as:

$$(1) \quad I(y,z) = \sum_{i=1}^{M}\sum_{j=1}^{N} A_{ij}(\tau_{ij,yz})$$

where

the time of flight (TOF) $\tau_{ij,yz}$ is the propagation time of the ray path from the transmitter $T_i(y_i, z_i)$ to the focus pixel $P(y, z)$ and back to the receiver $R_j(y_j, z_j)$.

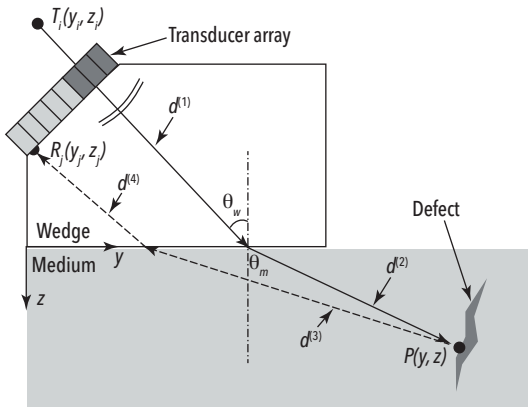

Figure 4. Ray tracing scheme connecting one virtual transmit element T_i, the focal point P, and one receiver element R_j.

Notice that the transmitter i can be a virtual source instead of a physical element if a subarray emission is considered (Lockwood et al. 1998). When a wedge is interposed between the transducer array and the test piece (as in the present case of the rail flaw imaging prototype), the wave path in the wedge must be taken into account in the beamforming algorithm. Referring to Figure 4, following Snell's law, the new backpropagation TOF can be calculated by finding the point of refraction at the wedge-medium interface (Sternini et al. 2019a, 2019b). Considering the fact that, in general, both L-waves and S-waves can propagate in the test medium, where only L-waves can be considered in the wedge, there exist, in general, up to four wave mode combinations that can be theoretically utilized for imaging. Accordingly, the backpropagation time $\tau_{ij,yz}$ for each of the possible wave mode combinations can be calculated as:

$$(2)\quad \tau_{ij,yz}^{LLLL,\ LLSL,\ LSLL,LSSL} = \frac{d_{i,yz}^{L(1)}}{c_w^L} + \frac{d_{i,yz}^{L,S(2)}}{c_m^{L,S}} + \frac{d_{j,yz}^{L,S(3)}}{c_m^{L,S}} + \frac{d_{j,yz}^{L(4)}}{c_w^L}$$

where

LLLL is <L-wave transmitted in wedge + L-wave refracted in medium + L-wave reflected in medium + L-wave received in wedge>,

LLSL is <L-wave transmitted in wedge + L-wave refracted in medium + S-wave reflected in medium + L-wave received in wedge>,

LSLL is <L-wave transmitted in wedge + S-wave refracted in medium + L-wave reflected in medium + L-wave received in wedge>,

LSSL is <L-wave transmitted in wedge + S-wave refracted in medium + S-wave reflected in medium + L-wave received in wedge>,

$c_m^{L,S}$ is the L-wave or S-wave velocity in the medium,

c_w^L is the L-wave velocity in the wedge, and

$d_{i,yz}^{L(1)}$, $d_{i,yz}^{L,S(2)}$, $d_{j,yz}^{L,S(3)}$, and $d_{j,yz}^{L(4)}$ are the corresponding propagation distances of each ray path segment as identified in Figure 4.

It was previously shown that the compounding of multiple wave modes can dramatically increase the array gain (Lanza di Scalea et al. 2017; Sternini et al. 2019a, 2019b). In this paper, only S-waves are considered in the rail steel because of the use of the shear wedge that maximizes S-wave refractions.

In order to generate the final image, the raw waveforms are analyzed via their Hilbert transform (analytical representation) as customary in SAF (Frazier and O'Brien 1998). Specifically, each waveform is decomposed into its in-phase and phase-quadrature components, and the final image is built by computing the modulus of these two contributions at each pixel $P(y, z)$.

Sparse SAF and Emission Using Subarrays

The general SAF scheme in full matrix capture (FMC) mode requires emitting from each individual element of the transducer array sequentially (one channel at a time) with the full aperture acting in reception for each transmission. However, utilizing all possible transmissions slows down the imaging process and increases the computational burden. That is why, particularly so in the medical imaging field, "sparse" transmission schemes are being considered to increase imaging speed without sacrificing image quality (Karaman et al. 1995). Since imaging speed is inversely proportional to the number of transmissions, the sparse SAF technique utilized in the rail flaw imaging prototype employs only a subset of all possible transmission events. In order to compensate for the limited energy transmissible by a single element at high frame rates, multiple elements (a subarray) are fired at once (Lockwood et al. 1998). As shown in Figure 5a, for example, an 8-element array only transmits three defocused circular waves using 3-element subapertures to replace eight consecutive firings of each element. In each transmit event i, the acoustic field of the phased subaperture elements superimposes a circular wavefront such that the transmission of the 3-element subaperture can be modeled as a virtual element (point source) placed behind the physical array. In the transmit beamforming, a virtual element array substitutes the physical transmit subapertures in the consideration of the DAS ray paths. As shown in Figure 5b, each transmit beam can be properly time delayed by calculating the ray path connecting the virtual array element and the focus point P, so that the three transmitted wave fronts are compounded coherently at an on-axis focus. By adjusting the time delays, the synthetic focus can be achieved at any point in the region of interest (ROI), such as an off-axis location in Figure 5c. The ability to dynamically focus the defocused beams at various locations ensures an acceptable resolution of the SAF images throughout the ROI. This is particularly important for the imaging of rail flaws since the size of the transverse-type defects can be fairly large compared to the physical aperture of the array, thus occupying the full height of the ROI. For the 64-element array in the imaging prototype, the authors have found that using eight, 17-element subarrays with a 9-element-wide pitch between virtual elements (the first and last firings have to discard part of the subaperture that is

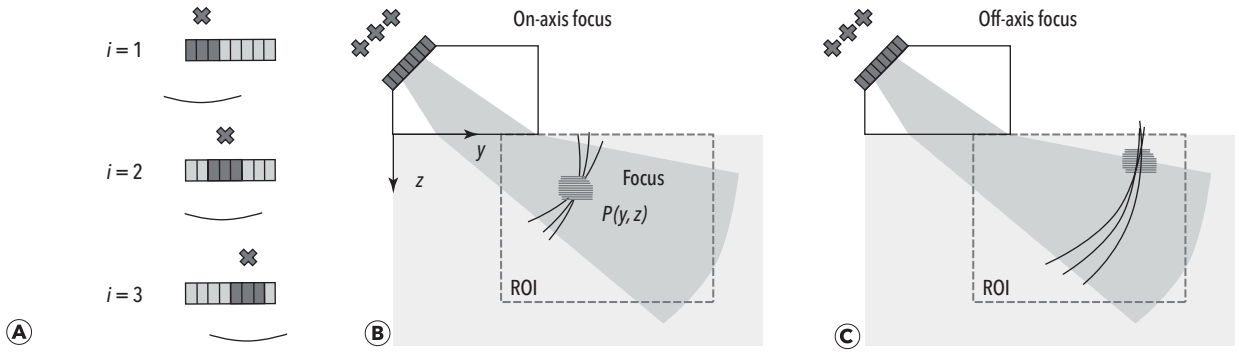

Figure 5. Subarray SAF technique for faster and more accurate images: (a) three defocused waves defined by the virtual elements are emitted independently by subarrays. Beamforming in transmission is performed by applying time delays corresponding to a synthetic focus on point *P* either at (b) on-axis positions or (c) off-axis positions.

beyond the physical array element numbers) is a reasonable compromise between imaging speed and image quality (resolution and signal-to-noise ratio [SNR]).

Quasi Real-Time Rail Flaw Image Display in 3D

The prototype includes a GUI that has been specifically designed for the rail flaw imaging application. After the setup configuration of the multiplexer, the user starts the scanning process by moving the probe along the transverse direction of the rail (perpendicularly to the imaging Y-Z plane). The parallel computation capability of GPU in the host computer achieves quasi real-time beamforming of the SAF images with a frame rate of ~25 Hz using an eight-transmission modality (Martin-Arguedas et al. 2012). The frame rate limit in the system comes from the data transmission and conversion hardware. The theoretical frame rate limit is much higher. As shown in Figure 6, the quasi real-time 3D point cloud display is created by compounding the beamformed 2D images at each transverse position tracked by the encoder. The raw 2D SAF image slices are displayed using a –30 dB threshold while the 3D display highlights only the pixels with intensity above the –15 dB threshold. To distinguish image slices of different signal strengths in the volumetric compounding, each 2D image is normalized by the maximum intensity value in the total collection of 3D pixels. Such a normalization process calibrates the decibel levels of "noised" image slices to those images with a strong reflection, suppressing any noise-only pixels between different image slices. In the 3D display, the algorithm performs this normalization adaptively by retaining the maximum intensity value from the previous 2D image and updating it if a larger maximum value is obtained. Notice that the temporary display of the 3D point cloud is only for an initial visualization of any strong reflections, including artifacts that could affect the final size estimation. A post-processing algorithm is needed to extract accurate quantitative information regarding a possible internal flaw.

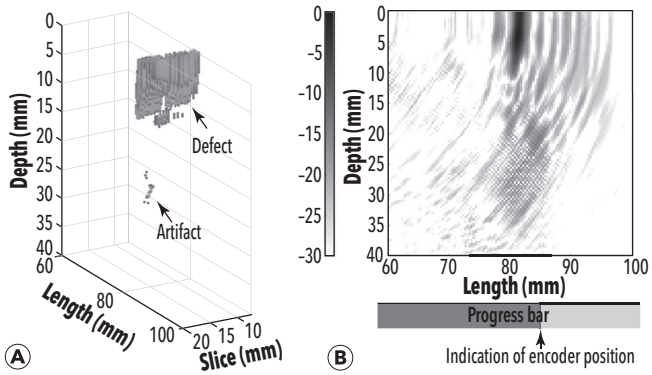

Figure 6. GUI runtime window displaying (a) compounded 3D point cloud (–15 dB) and (b) raw 2D SAF image (–30 dB). The refreshing rate is 25 Hz using the improved SAF technique.

Post-Processing of Volumetric SAF Images

Post-processing algorithms have been developed to further analyze the volumetric SAF images in order to extract the final size and shape of the flaw. The flowchart illustrating the steps taken in post-processing is shown in Figure 7. Referring to the schematic on the upper right, the SAF image slices are beamformed in the vertical plane, while the final plane of interest is the transverse plane. To prepare for image processing, the point cloud is first resized to high resolution through bilinear interpolation and converted from the decibel level (–40 to 0 dB) to an 8-bit grayscale, as shown in Figure 7a with two sample slices both in the vertical plane and the transverse plane. The volumetric image first goes through a coupled dilation-erosion operation, where the intensity of each pixel is first increased and then decreased based on the intensity distribution of the neighboring pixels in 3D. As shown in Figure 7b, the coupled morphology process blurs the void between the grating lobes that are caused by Rayleigh diffraction limit of the beamformed ultrasonic waves. Following the dilation and erosion operation, the volumetric image is flattened to an identified noise level through filtering techniques, as shown in Figure 7c. Each transverse plane slice is low-pass

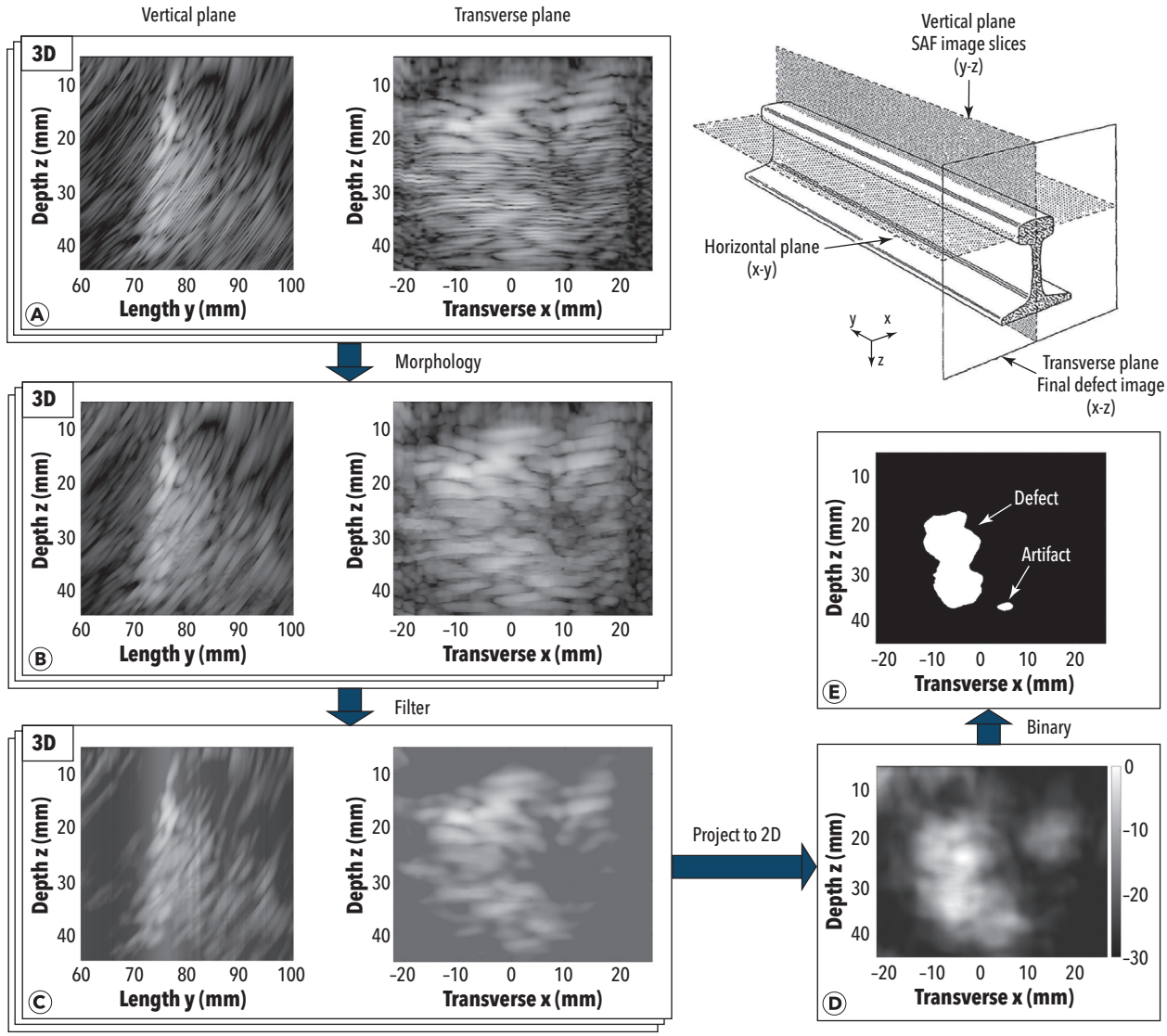

Figure 7. Volumetric image post-processing flowchart.

filtered and then subtracted from the original slice to flatten the noise "phantoms." From the sample slice in the vertical plane, the smoothing process does not change the intensity of the main lobe response. Since the noise floor is identified in each transverse plane, the volumetric intensity map can finally be projected onto the transverse plane such that the high intensity pixels are coherently added up, while the lower intensity pixels remain at their intensity levels. Shown in Figure 7d, after converting the grayscale image to decibel levels, the example transverse defect is finally identified with a high contrast.

At this point of the processing, it is necessary to isolate the flaw from the background image. The critical step to highlight the edge of the flaw is to apply a decibel level threshold and convert the intensity map into a binary map. Typically, the threshold is chosen as –15 dB for a ~30 dB dynamic range SAF image, but the value should be adaptive to various circumstances such as defect orientation, reflectivity, SNR, and so forth. In this paper a dynamic threshold level is determined through the following empirical equation:

$$\text{Threshold} = a + b^{*}\cos(\theta_{\text{defect}}) + c^{*}\text{noise} \quad (3)$$

where

$\{a, b, c\}$ are empirical constants calibrated from ground truth results from known flaws,

θ_{defect} is the incident angle of the acoustic beams on the flaw, and

noise is the decibel level of the background phantom determined in the flattening process.

To find the incident angle θ_{defect}, the algorithm first approximates the tilted angle φ of the flaw using the initial 3D

visualization by projecting the 3D cluster on arbitrary inclined transverse planes and finding the angle of the tentative plane that results in the maximum area of the defect. The incident angle is then computed by considering the geometric relationship between the broadside of the refracted acoustic beams and the defect inclination φ. As an example, consider a 30 dB dynamic range tomography of a sample transverse defect with an estimated inclination φ = 20°. The resulting incident angle θ_{defect} using the 55° shear wedge is 15°. A reasonable set of empirical constants is therefore a = 1.5, b = –2, and c = 0.5 to obtain a threshold of –15.4 dB. When the incident angle is small, it is appropriate to increase the search range in the decibel levels since the defect gives a good reflection to the array (higher contrast image), which results in a negative value of b. The additional consideration of noise level gives a second chance of energy level adjustment according to the image SNR.

The final binary defect image is shown in Figure 7e. Typically, for a single flaw present in the scanner area, a good SNR in SAF imaging results in only one cluster of pixels. However, as in the case of Figure 7e, a less than ideal SNR may result in artifacts that still need to be segmented out before the final estimation of the flaw size. For this purpose, the algorithm further segments the 3D point cloud using the k-means clustering algorithm by calculating a minimum Euclidean distance between pixels to form identified clusters. The minimum Euclidean distance is set to 1.4 mm (S-wave resolution in steel) to differentiate between different clusters of pixels, and the clusters are arranged in descending order per area. To account for cases of multiple separate flaws within the same scanned area, the GUI includes the possibility to investigate each individual cluster if the secondary clusters are worthy of attention.

Experimental Results

Validation of the rail flaw SAF imaging prototype was performed on flawed rail sections from the FRA defect library managed by MxV Rail. Some of the test sections contained natural rail defects, while others contained artificial defects. Following the scanning by the prototype at UCSD Experimental Mechanics & NDE Laboratory, each test rail section with natural defects was broken by MxV Rail personnel to establish the "ground truth" from visual observation of the flaws. Following the initial validation, some parameters in the SAF post-processing algorithms were optimized to better match the ground truth.

Figure 8 shows the final images obtained by the SAF imaging prototype for three natural defects from three FRA rail sections compared to the corresponding ground truth pictures after the rail breaks. Figure 8a shows the case of a natural transverse defect (TD) in a weld. In this case, the size and shape of the defect are perfectly imaged by the SAF system, with a size error as low as –2.3%. This example, therefore, shows an ideal case of a strong reflector (large SNR of the ultrasonic reflections) and located in a region that allowed good contact between the wedge and the rail surface during manual scanning. Figure 8b shows the case of a void defect in the welded region of another rail section. The ground truth picture shows a clear indication of the void with the oxidized boundary. However, compared to the first case of the TD, the void defect is a slightly weaker reflector of ultrasound. In the raw SAF images for this case, the noise level is as high as –25 dB, and some areas of the reflection from the weld may be mistaken for the defect in the initial 3D point cloud display. However, as shown in Figure 8b, the post-processing routine described in the previous section successfully isolates the void reflector with a final defect area estimation only differing

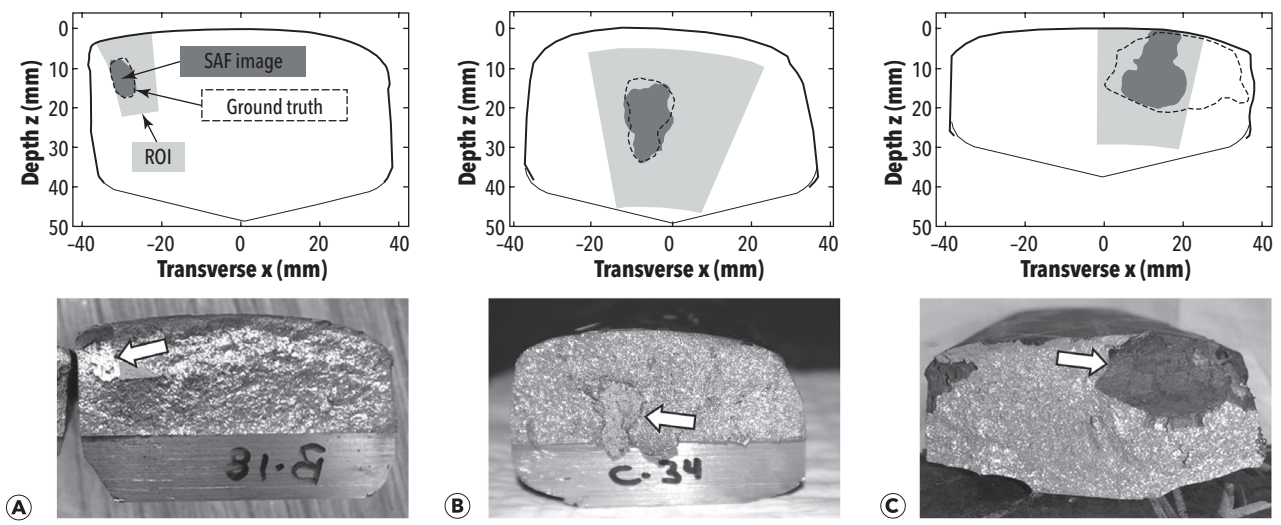

Figure 8. Validation tests. SAF images of natural rail flaws and their corresponding ground truth pictures: (a) a transverse defect in a weld; (b) a void in a weld; and (c) a transverse defect in the railhead corner.

from the ground truth by 3%, with a similarly good match in defect shape. Figure 8c shows the case of a natural TD located in the upper right corner of the railhead. This case highlights the difficulty in scanning defects located under highly curved surfaces such as the head corners. In this case, it is impossible to maintain good wedge-rail contact throughout the entire scan. As a consequence, the SNR of the SAF reflections degrades close to the head corners, making these regions effectively "blind" to the scanning. Due to the contact limitation, the final image of Figure 8c only shows about half of the defect, resulting in a severe underestimation of the defect size.

Figure 9 shows the validation results for four cases of artificial defects (end-drilled holes or EDHs) in the FRA defect library. In these cases, the ground truth is obtained from CAD drawings of the holes. Figure 9a shows an EDH in the railhead corner. Due to the aforementioned difficulty to maintain a good wedge-rail contact, the ROI cannot fully cover the corner defect, resulting in the expected size underestimation. When the EDH is in the middle of the railhead, as in Figure 9b, the SAF imaging results in a good match to the ground truth. In the absence of other explanations, the "leakage" of the SAF image at the bottom of the EDH is likely to be a secondary crack growing from the corner of the drill bit. Figure 9c shows an EDH in a heavily worn rail section. In this case, the wedge-rail contact is further compromised by the highly curved surface, resulting in a severe underestimation of the defect size. Finally, Figure 9d shows an EDH in a worn section with a sharp corner on the head surface. This is an extremely unideal case, since the scanning process has to stop before the probe reaches the corner to avoid complete loss of signal. It is comforting to see that even in cases of reduced ROI due to the rail corner curvature, the portion of the defect that is successfully scanned shows a good match with the corresponding portion of the ground truth holes.

Discussion and Conclusion

SAF techniques are the new front in ultrasonic imaging of internal discontinuities because of their potential for accurate and fast imaging. This paper has presented a portable prototype based on SAF techniques applied to the 3D imaging of rail flaws. This tool can improve the outcome of the manual verification of rail flaws by resulting in objective flaw size and shape that can then inform the most appropriate remedial actions. The prototype is hosted in a ruggedized carry-on size case and is battery powered for autonomous operation. The sensing probe consists of a linear ultrasonic array that is mounted on a wedge and includes a position encoder to build 3D images from 2D SAF slices. The beamforming algorithm tracks the ray paths of the ultrasonic waves through the wedge and utilizes sophisticated subarray sparse firing to increase imaging speed. Currently, high-contrast images can be obtained at a frame rate of 25 Hz, although higher speeds can be obtained (if necessary) by further reducing the number of firings at the expense of image quality. Special post-processing algorithms are utilized to reduce the 3D point cloud into a result that can lead to the final size and shape of one (or multiple) flaws present in the scanned ROI.

The imaging prototype was tested on rail sections containing both natural and artificial flaws from the FRA rail defect library managed by MxV Rail (formerly TTCI). The testing allowed the authors to refine some control parameters of the imaging system to find the best match to the ground truth. Good results, in terms of both flaw size and flaw shape, were obtained in the presence of natural TDs and EDHs if the defects were located some distance from the railhead corners. When instead the defects were located underneath the head corners (and particularly so in the presence of heavy head wear), the curvature of the surface adversely affected the wedge-rail contact, effectively reducing the scanned ROI. In

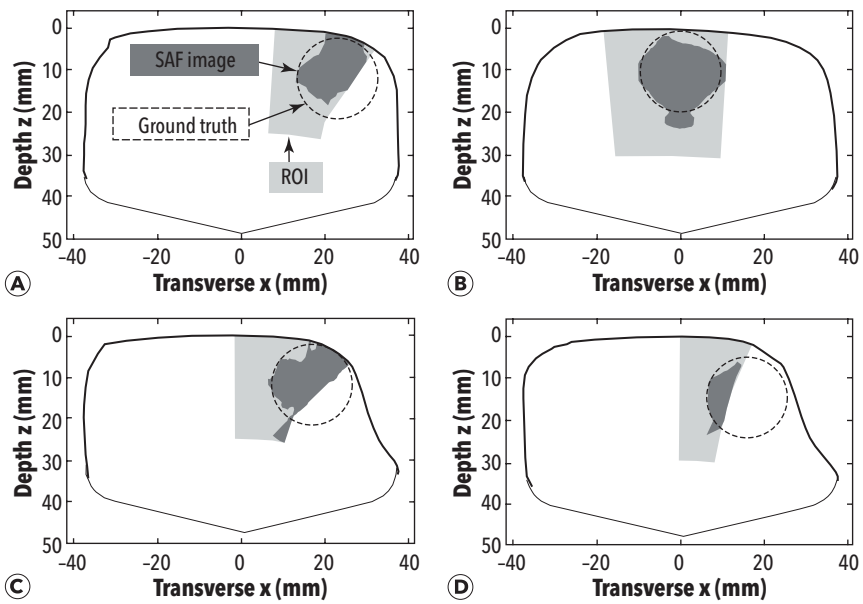

Figure 9. Validation tests. SAF images of artificial rail flaws (end-drilled holes [EDHs]) and their corresponding ground truth circles: (a) EDH in railhead corner; (b) EDH in middle of railhead; (c) and (d) EDH in heavily worn railhead corner.

these cases, therefore, only a portion of the flaw could be successfully scanned, resulting in an underestimation of flaw size.

Further work should be devoted to adapting the sensing probe to enable scanning on curved surfaces, which could be accomplished using either conformable wedges or fully stretchable and flexible transducer arrays, as recently demonstrated by one of the authors and collaborators (Hu et al. 2018). This is an area of open research.

While the primary goal of the present research is to improve current hand verification techniques for rail flaws, the fast SAF technique introduced here could also be implemented in motion. Possibilities for in-motion imaging could be a walking-stick wheel or even an inspecting hi-railer vehicle, although important issues such as fast image data interpretation and full rail coverage (probably requiring multiple arrays simultaneously) would have to be addressed.

ACKNOWLEDGMENTS

This research was funded by the US Federal Railroad Administration under contract no. 693JJ619C000008 (Dr. Robert Wilson, Program Manager). The authors acknowledge the technical feedback provided by Dr. Wilson throughout this project. The authors also acknowledge the support of the former Transportation Technology Center (now MxV Rail) in Pueblo, Colorado, and especially Dr. Anish Poudel, for providing the rail test sections utilized in the validation tests and the ground truth information, as well as assisting with the evaluation of the results. Finally, the authors would like to acknowledge Mr. Gavin Dao of Advanced OEM Solutions (West Chester, OH) for providing technical advice on SAF hardware solutions and valuable insights over the use of the multiplexer currently adopted in the prototype.

REFERENCES

Drinkwater, B. W., and P. D. Wilcox. 2006. "Ultrasonic arrays for non-destructive evaluation: A review." *NDT & E International* 39 (7): 525–41. https://doi.org/10.1016/j.ndteint.2006.03.006.

Flaherty, J. J., K. R. Erikson, and V. M. Lund. 1967. Synthetic aperture ultrasonic imaging systems. U.S. Patent 3,548,642, filed 2 March 1967, and issued 22 December 1970.

Frazier, C. H., and W. D. O'Brien. 1998. "Synthetic aperture techniques with a virtual source element." *IEEE Transactions on Ultrasonics, Ferroelectrics, and Frequency Control* 45 (1): 196–207. https://doi.org/10.1109/58.646925.

Hu, H., X. Zhu, C. Wang, L. Zhang, X. Li, S. Lee, Z. Huang, et al. 2018. "Stretchable ultrasonic transducer arrays for three-dimensional imaging on complex surfaces." *Science Advances* 4 (3): eaar3979. https://doi.org/10.1126/sciadv.aar3979.

Huang, C., and F. Lanza di Scalea. 2022. "High Resolution Real Time Synthetic Aperture Imaging in Solids Using Virtual Elements," *Proceedings of the ASME 2022 International Mechanical Engineering Congress and Exposition. Volume 9: Mechanics of Solids, Structures, and Fluids; Micro- and Nano-Systems Engineering and Packaging; Safety Engineering, Risk, and Reliability Analysis; Research Posters*. https://doi.org/10.1115/IMECE2022-94445.

Jensen, J. A., S. I. Nikolov, K. L. Gammelmark, and M. H. Pedersen. 2006. "Synthetic aperture ultrasound imaging." *Ultrasonics* 44 (Suppl. 1): e5–15. https://doi.org/10.1016/j.ultras.2006.07.017.

Karaman, M., P. -C. Li, and M. O'Donnell. 1995. "Synthetic aperture imaging for small scale systems." *IEEE Transactions on Ultrasonics, Ferroelectrics, and Frequency Control* 42 (3): 429–42. https://doi.org/10.1109/58.384453.

Lockwood, G. R., J. R. Talman, and S. S. Brunke. 1998. "Real-time 3-D ultrasound imaging using sparse synthetic aperture beamforming." *IEEE Transactions on Ultrasonics, Ferroelectrics, and Frequency Control* 45 (4): 980–88. https://doi.org/10.1109/58.710573.

Lanza di Scalea, F., 2007, "Ultrasonic testing applications in the railroad industry," Chapter 15: *Special Applications of Ultrasonic Testing*, in *Non-destructive Testing Handbook*, 3rd edition, P.O. Moore, ed., American Society for Nondestructive Testing, pp. 535-552.

Lanza di Scalea, F., S. Sternini, and T. V. Nguyen. 2017. "Ultrasonic imaging in solids using wave mode beamforming." *IEEE Transactions on Ultrasonics, Ferroelectrics, and Frequency Control* 64 (3): 602–16. https://doi.org/10.1109/TUFFC.2016.2637299.

Martin-Arguedas, C. J., D. Romero-Laorden, O. Martinez-Graullera, M. Perez-Lopez, and L. Gomez-Ullate. 2012. "An ultrasonic imaging system based on a new SAFT approach and a GPU beamformer." *IEEE Transactions on Ultrasonics, Ferroelectrics, and Frequency Control* 59 (7): 1402–12. https://doi.org/10.1109/TUFFC.2012.2341.

Sternini, S., A. Y. Liang, and F. Lanza di Scalea. 2019a. "Ultrasonic synthetic aperture imaging with interposed transducer–medium coupling path." *Structural Health Monitoring* 18 (5-6): 1543–56. https://doi.org/10.1177/1475921718805514.

Sternini, S., A. Y. Liang, and F. Lanza di Scalea. 2019b. "Rail Defect Imaging by Improved Ultrasonic Synthetic Aperture Focus Techniques." *Materials Evaluation* 77 (7): 931–40.

Witte, M., and A. Poudel. 2016. "High-speed rail flaw detection using phased array ultrasonics." *Technology Digest TD16-030*.